IOP Publishing

Smart Materials and Structures

Smart Mater. Struct. 30 (2021) 015029 (10pp)

https://doi.org/10.1088/1361-665X/abc7fa

Graded multifunctional piezoelectric metastructures for wideband vibration attenuation and energy harvesting

M Alshaqaq and A Erturk

G.W. Woodruff School of Mechanical Engineering, Georgia Institute of Technology, Atlanta GA 30332, United States of America

E-mail: alper.erturk@me.gatech.edu

Received 3 September 2020, revised 16 October 2020
Accepted for publication 5 November 2020
Published 9 December 2020

Abstract

Unlike well-studied locally resonant (LR) metamaterials with a periodic array of identical resonators, 'graded' LR metamaterials consist of an array of resonators with a spatially varying parameter, yielding wideband wave attenuation and mode trapping/localization, among other features. In this work, we explore a graded LR piezoelectric metamaterial-based structure (i.e. metastructure) in which the grading parameter, namely the inductive shunt resonant frequency of the unit cells, follows a predefined variation pattern in space (e.g. first-order, quadratic, or fractional). We investigate the effect of such patterns on (i) the vibration attenuation bandwidth, (ii) the localization of vibration modes, and (iii) the harvested power. To this end, we consider a piezoelectric bimorph cantilever hosting an array of piezoelectric unit cells with spatially varying inductive shunts. Fully coupled electromechanical equations describing the metastructure's linear transverse displacement and unit cell voltages are given with a modal analysis framework and solved using the matrix inversion method. The results show that (i) the first-order grading pattern yields the widest bandgap with 65% increase in the bandwidth compared to the standard uniform LR pattern, (ii) the localization of vibration modes follows in shape the corresponding frequency grading pattern, and (iii) the largest power is harvested for the fractional grading pattern. Furthermore, all of the graded resonator configurations result in wider bandwidth in energy harvesting as compared to the uniform resonators case. Overall, the results unveil the fundamental characteristics of this class of graded piezoelectric metastructures and support the design of such multifunctional piezoelectric metastructures for concurrent vibration attenuation and energy harvesting.

Keywords: metamaterial, piezoelectric, vibration attenuation, energy harvesting

(Some figures may appear in colour only in the online journal)

1. Introduction

The discovery of locally resonant metamaterials [1] has inspired researchers over the past two decades to investigate various elastic and acoustic metamaterial configurations with resonating unit cells. Locally resonant metamaterials (and resulting finite *metastructures* with specified boundary conditions) yield exotic dynamics such as negative effective mass [2–4], negative effective stiffness [5, 6], or a combination of both in hybrid configurations [7]. One important feature of such locally resonant metastructures is the ability to form a low-frequency *bandgap*, i.e. frequency range in which wave propagation is forbidden for wavelengths much longer than the lattice parameter. In contrast to frequency bandgaps formed by Bragg scattering (in phononic crystals) which are not practical for filtering waves in the low-frequency range, locally resonant bandgaps can be designed to create attenuation at low frequencies. As a result, locally resonant metastructures have been widely explored for vibration attenuation, albeit the bandgap size is relatively limited by the added mass of the resonators [4].

Researchers have theoretically and experimentally investigated a number of different strategies to widen the bandgap of locally resonant metastructures. Some of these strategies include the use of: (i) multi-degree-of-freedom local resonators [8] in rods [9], plates [10–12] and beams [13–15] to create multiple bandgaps; (ii) multiple periodic arrays of single-degree-of-freedom local resonators [16–18] to create multiple bandgaps or a single broadband bandgap; (iii) internal coupling between two neighboring local resonators [19–21] in which three separate bandgaps can be formed due to the coupling effect; (iv) Bragg-type and resonance-type bandgap combination [22–25] to increase the bandwidth; (v) tunable resonators such as shape memory alloy [26, 27], dielectric elastometer [28–30], and piezoelectric shunting [14, 31, 32] to control and widen the bandgap; (vi) non-linear local resonators to increase the bandgap width [33–35], and (vii) quasiperiodic arrangement of local resonators to create additional, non-trivial, bandgaps [36].

While many studies have investigated locally resonant metastructures with a periodic array of identical resonating elements, more recently a new class of metamaterials has emerged by incorporating resonators with gradually varying properties to achieve enhanced wave manipulation capabilities. These modified locally resonant metamaterial-based structures are *graded metastructures* (the word 'graded' refers to the smooth variation of a particular parameter of the local resonators). Graded metastructures have attracted increasing attention due to their ability to manipulate waves, for example, localization of waves over some spatial region along the structure as well as enabling wideband vibration attenuation. Specifically, the trapping of waves with different frequency content at different spatial positions is often referred to as *rainbow trapping* following the pioneering work in electromagnetics and plasmonics [37, 38], which was later implemented for acoustic [39] and elastic waves [40].

Because piezoelectric resonators are easy to implement and tune [41–44], they also have been used in this context with spatially varying shunts. Thomas *et al* [45] proposed an optimization method to tune the target frequency of each shunt circuit to achieve a wider bandgap. Recently, Hu *et al* [46] showed vibration attenuation improvement in piezoelectric metastructures with first-order graded local resonators in which the linear grading of local resonators was achieved by tuning the corresponding capacitance of individual shunt circuits. Elastic waves propagating in graded metastructures can be trapped at some location along the structure, implying that the vibration energy is also trapped over the same region and with a relatively wider frequency band (compared to uniformly periodic arrangements). As a result, researchers have leveraged this wave trapping phenomenon to enhance energy harvesting, particularly in the spatial region where waves are trapped, as done in the papers by De Ponti *et al* [9, 47] and Chaplain *et al* [48].

In the existing literature, graded metamaterials and metastructures with a first-order graded array of local resonators have been given most attention, especially in terms of the vibration attenuation. In the present work, we explore a graded metastructure in which the graded array of local resonators follow shunt resonant frequency grading patterns toward understanding the simultaneous effects on the (i) vibration response, (ii) mode localization, and (iii) energy harvesting capabilities. Specifically, we study locally resonant electromechanical metastructures hosting a graded array of shunted piezoelectric elements tuned to slightly different target frequencies that follow specific spatial distributions (i.e. the grading parameter is the frequency of shunt circuits). In section 2, the electromechanical governing equations are summarized based on modal analysis, and select graded frequency patterns are outlined, namely: (i) fractional, (ii) first-order, and (iii) high-order (e.g. quadratic) frequency grading patterns. In section 3, numerical results are presented to reveal the effect of different graded frequency patterns in the form of beam tip transmissibility and real power output plots. Finally, in section 4 we draw some remarks.

2. Theoretical background

Consider a cantilever bimorph piezoelectric beam under harmonic base excitation covered by S pairs of segmented electrodes with negligible thickness. The bimorph piezoelectric layers are connected in series and each segmented electrode pair forms a unit cell that is connected to a parallel resistive-inductive shunt circuit as shown in figure 1. For uniform locally resonant piezoelectric metastructures, all unit cells are connected to identical shunt circuits with resonant frequency ω_t, but for the graded locally resonant piezoelectric metastructure considered here, the unit cells are connected to different shunt circuits tuned to gradually varying target frequencies that follow some predefined pattern as will be shown later. The composite beam is modeled using the Euler–Bernoulli theory in which rotary inertia and shear deformation are neglected. The cantilever beam is assumed to be undamped and modal damping will be added at a later stage.

The governing electromechanical equations for linear transverse vibration of the beam under harmonic base excitation and current balance in electrical shunt circuits are [6]

$$EI\frac{\partial^4 w}{\partial x^4} + m\frac{\partial^2 w}{\partial t^2} - \theta\sum_{j=1}^{S} v_j(t)\frac{d^2}{dx} \times [H(x - x_j^L) - H(x - x_j^R)] = -m\frac{d^2 w_b}{dt^2}, \tag{1}$$

$$C_{p,j}\frac{dv_j}{dt} + Y_j v_j(t) + \theta\int_{x_j^L}^{x_j^R}\frac{\partial^3 w}{\partial x^2, \partial t} = 0, \tag{2}$$

where j goes from 1 to S, $w(x,t)$ is the transverse vibration of the beam relative to the transverse base motion $w_b(t)$; $v_j(t)$ and

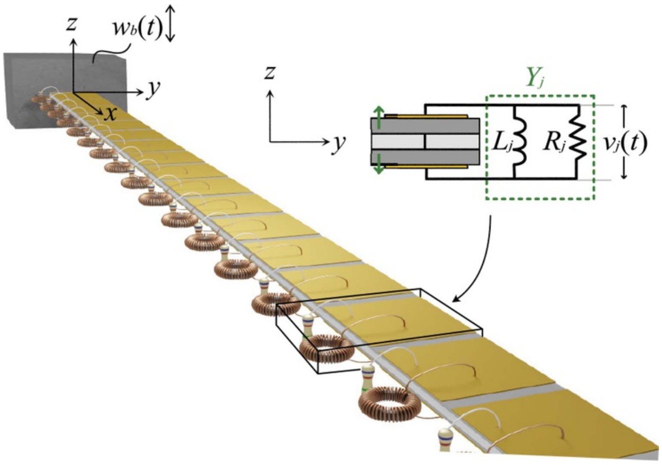

Figure 1. Schematic of a graded multifunctional piezoelectric metastructure under harmonic base excitation. The piezoelectric layers in each unit cell are connected in series. The close up shows the *j*th unit cell shunted to a resistive-inductive circuit and the little green arrows show the poling directions.

Y_j are, respectively, the voltage and the external load admittance across the *j*th electrode pair and $H(x)$ is the Heaviside function. Also, EI is the short-circuit flexural rigidity, m is the mass per unit length, θ is the electromechanical coupling term, and $C_{p,j}$ is the inherent piezoelectric capacitance across the *j*th electrode pair, defined as

$$EI = \frac{2b}{3}\left(c_s\frac{h_s^3}{8} + \bar{c}_{11}^E\left[\left(h_p + \frac{h_s}{2}\right)^3 - \frac{h_s^3}{8}\right]\right), \tag{3}$$

$$m = b(\rho_s h_s + 2\rho_p h_p), \tag{4}$$

$$\theta = \frac{\bar{e}_{31} b_e}{2h_p}\left[\left(h_p + \frac{h_s}{2}\right)^2 - \frac{h_s^2}{4}\right], \tag{5}$$

$$C_{p,j} = \bar{\varepsilon}_{33}^S b_e \frac{(x_j^R - x_j^L)}{2h_p}. \tag{6}$$

Note that the width of each segmented electrode b_e is identical to the beam's width b and the other parameters in equations (3)–(6) are defined in table 1. Furthermore, the effective material properties reduced from the 3D constitutive equations are given by (the overbar indicates average properties calculated for 1D thin beams)

$$\bar{c}_{11}^E = \frac{1}{s_{11}^E}, \quad \bar{e}_{31} = \frac{d_{31}}{s_{11}^E}, \quad \bar{\varepsilon}_{33}^S = \bar{\varepsilon}_{33}^T - \frac{d_{31}^2}{s_{11}^E}. \tag{7}$$

To solve equations (1) and (2) we use the assumed modes method with N number of modes and write the transverse vibration of the beam as

$$w(x,t) = \sum_{r=1}^{N} \phi_r(x)\eta_r(t), \tag{8}$$

Table 1. Composite beam properties. The overbars indicate equivalent material properties for one-dimensional thin beams.

Parameter	Definition
Composite beam	
b	Width
L_b	Length
Substructure	
c_s	Elastic modulus
ρ_s	Mass density
h_s	Thickness
Piezoelectric layers	
ρ_p	Mass density
h_p	Thickness
$\bar{c}_{11}^E$	Elastic modulus at constant electric field
$\bar{\varepsilon}_{33}^S$	Permittivity component at constant strain
$\bar{e}_{31}$	Effective piezoelectric stress constant
s_{11}^E	Elastic compliance at constant electric field
d_{31}	Strain constant
$\bar{\varepsilon}_{33}^T$	Permittivity component at constant stress

where $\phi_r(x)$ are the undamped short-circuit mode shapes of the transverse motion of the beam and $\eta_r(t)$ are the modal coordinates. The mode shapes are normalized such that

$$\int_0^{L_b} m\phi_r(x)\phi_s(x)\mathrm{d}x = \delta_{rs}, \quad r,s = 1,2,..., \tag{9}$$

$$\int_0^{L_b} EI\phi_r(x)\frac{d^4\phi_s(x)}{dx^4}\mathrm{d}x = \omega_r^2\delta_{rs} \quad r,s = 1,2,... \tag{10}$$

Substituting equation (8) into equation (1), multiplying by the mode shape $\phi_k(x)$, applying orthogonality condition, and integrating over x from 0 to L_b (see Sugino *et al* [6] for more details), and introducing modal viscous damping, yields

$$\frac{d^2\eta_r}{dt^2} + 2\zeta_r\omega_r\frac{d\eta_r}{dt} + \omega_r^2\eta_r - \theta\sum_{j=1}^{S} v_j \left.\frac{d\phi_r}{dx}\right|_{x_j^L}^{x_j^R} = q_r(t), \tag{11}$$

$$C_{p,j}\frac{dv_j}{dt} + Y_j v_j + \theta\sum_{r=1}^{N}\frac{d\eta_r}{dt}\left.\frac{d\phi_r}{dx}\right|_{x_j^L}^{x_j^R} = 0, \tag{12}$$

where r goes from 1 to N and j goes from 1 to S, and

$$q_r(t) = -m\frac{d^2 w_b}{dt^2}\int_0^{L_b}\phi_r(x)\mathrm{d}x \tag{13}$$

is the modal forcing due to some arbitrary base motion. Taking Laplace transforms of equations (11) and (12) and assuming harmonic base excitation, the governing equations for modal coordinates and voltages become

$$(s^2+2\zeta_r\omega_r s+\omega_r^2)H_r(s)+s\theta^2\sum_{j=1}^{S}\frac{1}{C_{p,j}\,(s+h_j(s))}\frac{d\phi_r}{dx}\bigg|_{x_j^L}^{x_j^R}\times\sum_{k=1}^{N}\frac{d\phi_k}{dx}\bigg|_{x_j^L}^{x_j^R}H_k(s)=Q_r(s),\tag{14}$$

$$(sC_{p,j}+Y_j(s))\,V_j(s)+s\theta^2\sum_{r=1}^{N}\frac{1}{s^2+\omega_r^2}\frac{d\phi_r}{dx}\bigg|_{x_j^L}^{x_j^R}\times\sum_{k=1}^{S}\frac{d\phi_r}{dx}\bigg|_{x_k^L}^{x_k^R}V_k(s)=Q_j(s),\tag{15}$$

where $H(s)$ and $V(s)$ are, respectively, the Laplace transforms of $\eta(t)$ and $v(t)$, and

$$h_j(s)=\frac{Y_j(s)}{C_{p,j}}\tag{16}$$

is the normalized admittance across the jth unit cell. Equations (14) and (15) form a system of $N+S$ coupled ordinary differential equations which can be solved using the matrix inversion method.

In the present study, unlike the uniform purely inductive shunts case [6], the unit cells are connected to *different* inductive shunt circuits in which resistors are also placed (in parallel), respectively, to explore resonant frequency grading as well as to enable simultaneous vibration attenuation and energy harvesting. Thus, the admittance across the jth unit cell is

$$Y_j(s)=\frac{1}{sL_j}+\frac{1}{R_j},\tag{17}$$

where R_j and L_j are the resistance and inductance of the jth shunt circuit, respectively. Substituting equation (17) into (16) yields

$$h_j(s)=\frac{\omega_{t,j}^2}{s}+\frac{1}{\tau_j},\tag{18}$$

where

$$\omega_{t,j}=\sqrt{\frac{1}{C_{p,j}L_j}}\tag{19}$$

is the resonant frequency of the jth shunt circuit and $\tau_j=C_{p,j}R_j$ is its time constant. It is clear that the resonant frequency of each shunt circuit can vary according to its respective inductance and capacitance values, however, we assume that the inherent capacitance of all segmented electrodes to be identical. Thus, the target resonant frequency of each shunt circuit is tuned by altering the values of the associated inductors only.

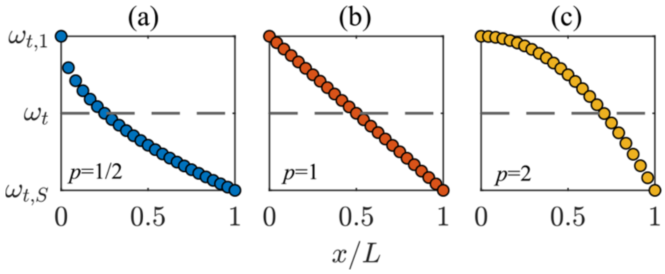

Figure 2. Target frequencies of the shunt circuits that are connected to segmented electrodes along the beam length showing (a) fractional ($p=1/2$), (b) first-order ($p=1$) and (c) quadratic ($p=2$) frequency grading patterns. First-order grading displays uniform frequency spacing between neighboring shunt circuits. $\Delta\omega$ is positive, yielding descending frequencies.

We consider different frequency grading patterns for the shunt circuits such that

$$\omega_{t,j}=\omega_t+\Delta\omega-2\Delta\omega\left(\frac{j-1}{S-1}\right)^p,\tag{20}$$

where ω_t is some target frequency around which gradual variation of the shunt circuit frequencies take place, and $2\Delta\omega$ defines the range of the frequency grading pattern. Note that positive values of $\Delta\omega$ result in a descending frequency grading such that the target frequency of the first shunt circuit (near the clamped end) is $\omega_{t,1}=\omega_t+\Delta\omega$ and that of the the last shunt circuit (near the free end) $\omega_{t,S}=\omega_t-\Delta\omega$. When $\Delta\omega$ is negative, the result is an ascending frequency grading pattern. The power p defines the profile of the frequency grading between the first and the last shunt circuits as illustrated in figure 2. Throughout the rest of the paper, fractional, first-order and high-order refer to frequency grading patterns with $0<p<1$, $p=1$ and $p>1$, respectively.

For a uniform locally resonant piezoelectric metastructure with a constant length, under the assumption of infinite (i.e. sufficiently large) number of unit cells connected to identical inductive shunt circuits tuned to the same target frequency ω_t, the bandgap width is calculated by Sugino *et al* [6] as

$$\frac{\omega_t}{\sqrt{1+\alpha}}<\omega<\omega_t,\tag{21}$$

where

$$\alpha=\frac{2\theta^2h_p}{EI\bar{\varepsilon}_{33}^{S}b_e}\tag{22}$$

is a dimensionless parameter quantifying the electromechanical coupling of the metastructure [6]. Note that, for graded locally resonant metastructures, the resulting bandgap width cannot be expressed in a form similar to equation (21), because a closed-form solution of equation (14) is beyond reach even for infinite resonators approximation. However, in order to facilitate the comparison of different graded frequency patterns, we need to establish a criterion. For this purpose, we adopt the approach in [49], where anything below 0.1 in the

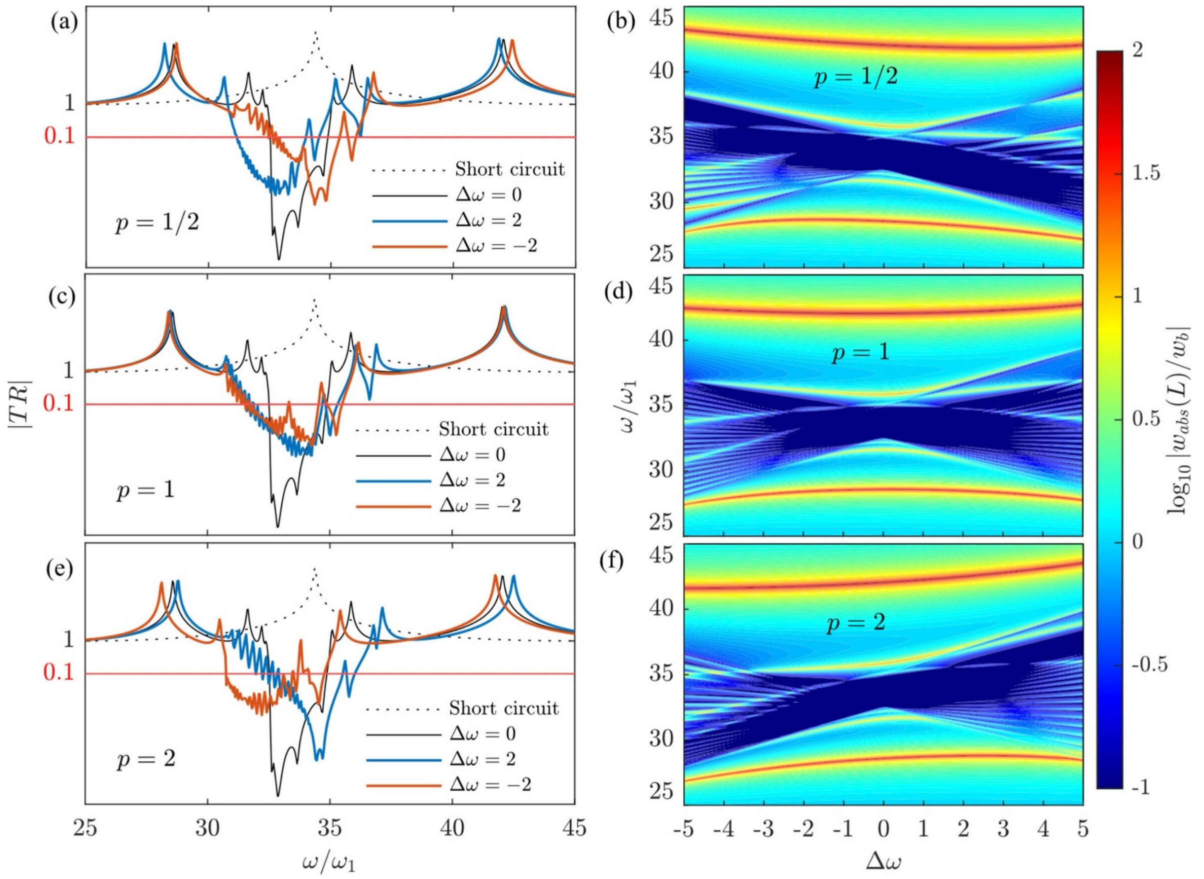

Figure 3. Transmissibility heatmaps versus normalized excitation frequency and dimensionless frequency range for (b) fractional ($p = 1/2$), (d) first-order ($p = 1$) and (f) quadratic ($p = 2$) frequency grading patterns. (a), (c) and (e) show tip transmissibility versus normalized excitation frequency for some selected frequency range values. $\Delta\omega = 0$ corresponds to the uniform frequency pattern. $S = 25$, $N = 200$, $\tau\omega_t = 500$, and $\zeta_r = 0.001$ are used.

beam tip transmissibility was considered as bandgap. The beam tip transmissibility is the ratio of the displacement at the free end of the beam to the displacement at its base (clamped end), given as

$$|\mathrm{TR}(\omega)| = \left|\frac{w_{abs}(L_b)}{w_b}\right|. \tag{23}$$

Then, the 'bandgap' (with a relatively relaxed definition) is achieved when

$$|\mathrm{TR}(\omega)| \leq 0.1 \tag{24}$$

is satisfied.

3. Case studies and results

We consider a bimorph cantilever made of aluminum substructure and piezoelectric ceramic PZT-5A with the properties listed in table 2. There are many factors involved in defining the frequency grading pattern such as the frequency range $2\Delta\omega$, the power p, and the number of unit cells S. However, based on the work of Sugino *et al* [6], a uniform locally resonant piezoelectric metastructure with $S = 10$ unit cells would be sufficient to ensure the formation of the bandgap. In order to rule out any effect of small number of unit cells, we will consider $S = 25$ unit cells throughout the numerical analysis. Also a target frequency of $\omega_t = 35\omega_1$ is assumed, where ω_1 is the first short-circuit resonant frequency of the composite beam, and a small structural damping ratio of $\zeta_r = 0.001$ is considered throughout the numerical results.

Table 2. Geometric and material properties of the graded multifunctional piezoelectric metastructure.

Parameter	Value	Unit
Composite beam		
b	10	mm
L_b	100	mm
Aluminum		
h_s	0.1	mm
c_s	69	GPa
ρ_s	2700	kg m^{-3}
PZT-5A		
ρ_p	7750	kg m^{-3}
h_p	0.3	mm
$\bar{c}_{11}^E$	61	GPa
$\bar{\varepsilon}_{33}^S$	13.3	nF m^{-1}
$\bar{e}_{31}$	−12.3	C m^{-2}

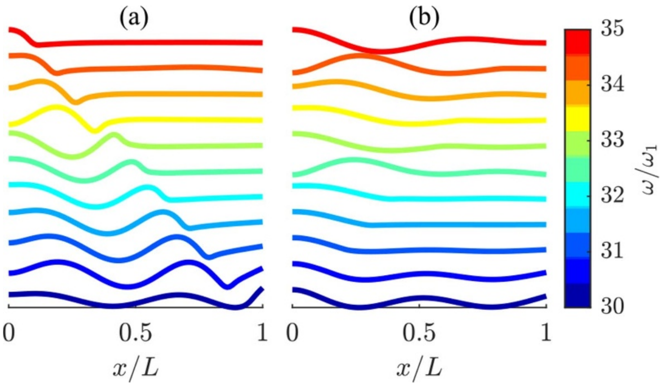

Figure 4. Steady state response profiles at different normalized excitation frequencies (30–35) within the bandgap for (a) decreasing and (b) increasing first-order frequency grading ($p = 1$). Note that (a) shows mode localization near the clamped end of the beam. $S = 25$, $N = 200$, $\Delta\omega = 2$, $\tau\omega_t = 500$, and $\zeta_r = 0.001$ are used.

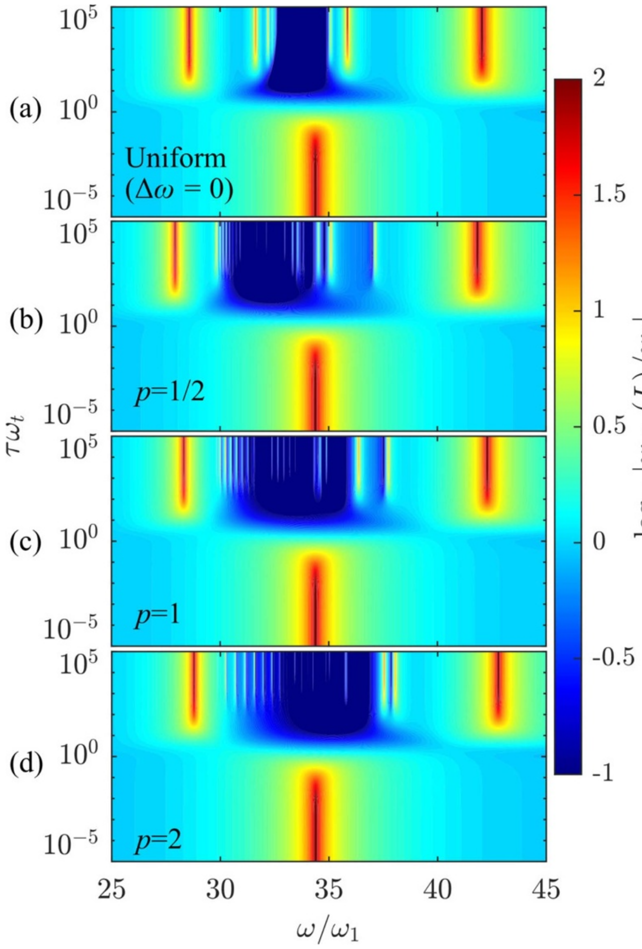

Figure 5. Beam tip transmissibility heatmaps versus normalized excitation frequency and dimensionless load resistance for (a) uniform, (b) fractional ($p = 1/2$), (c) first-order ($p = 1$) and (d) quadratic ($p = 2$) frequency grading patterns. $\Delta\omega = 3$, $S = 25$, $N = 200$, and $\zeta_r = 0.001$ are used.

3.1. Effect of frequency grading range

The frequency grading range defines the upper and the lower bounds of the frequency grading patterns shown in figure 2. It is important to investigate the optimal value of the frequency range that maximizes the vibration attenuation region (i.e. the widest bandgap that satisfies equation (24)). Figures 3(b), (d) and (f) show tip transmissibility heatmaps versus frequency range and normalized excitation frequency for the cases of $p = 1/2$, $p = 1$ and $p = 2$, respectively. We observe the following from the figures: (i) as the absolute value of the frequency range increases, the bandgap becomes wider until reaching a certain frequency range value where the bandgap splits into multiple gaps, (ii) positive frequency range values exhibit fewer gaps while negative frequency range values exhibit more gaps, and (iii) for positive frequency range values, quadratic frequency grading (figure 3(f)) shows bandgaps at higher frequencies while for negative frequency range values, bandgaps occur at lower frequencies; on the other hand, for fractional frequency grading, positive frequency range values show bandgaps at lower frequencies while negative frequency range values show bandgaps at higher frequencies; first-order frequency grading shows symmetric bandgaps.

These subtle differences in the bandgap formation for positive and negative frequency range values are captured in the associated tip transmissibility plots (figures 3(a), (c) and (e)). For the first-order frequency grading ($p = 1$), and regardless of the direction of grading, the bandgap occurs over approximately the same frequency range, though not identically. For quadratic ($p = 2$) and fractional ($p = 1/2$) frequency gradings, ascending and descending patterns yield bandgaps at two different regions. Note that the attenuation intensity inside the bandgap is stronger for the quadratic profile due to small frequency spacing between neighboring shunt circuits near the clamped end of the beam. One can clearly observe that the tip transmissibility curves are not identical for ascending and descending patterns. If identical shunt circuits are assumed, the bandgap would form to the left of the target frequency of the shunt circuits. Thus, having descending frequency grading patterns ensure that the target frequency of the neighboring shunt circuit (to the right) lies within the bandgap formed by the other shunt circuit (the one to the left) and this ensures overlapping of the individual bandgaps such that the result is a single continuous attenuation in the transmissibility curve (given small frequency spacing) with a few resonant peaks. These observations are valid and can be enhanced when the shunt circuits have some resistance (as in our case) such that the resonant peaks inside the bandgap are eliminated (or minimized). Based on these observations, only descending patterns can gradually slow down waves, trapping the elastic waves at some specific spatial region. This is clear in the tip transmissibility plots, where the descending pattern results in a gradual formation of bandgaps (blue line) while the ascending pattern suddenly forms the bandgap (lower bound) and hence no trapping of waves along the beam are observed. To further illustrate this, figure 4 shows the evolution of the steady state wave profile at some select normalized excitation frequencies inside the bandgap (from 30 to 35) for the case of first-order grading pattern ($p = 1$). It is clear that the descending grading pattern results in localized vibration modes, in which vibration energy is confined over some specific spatial region along the

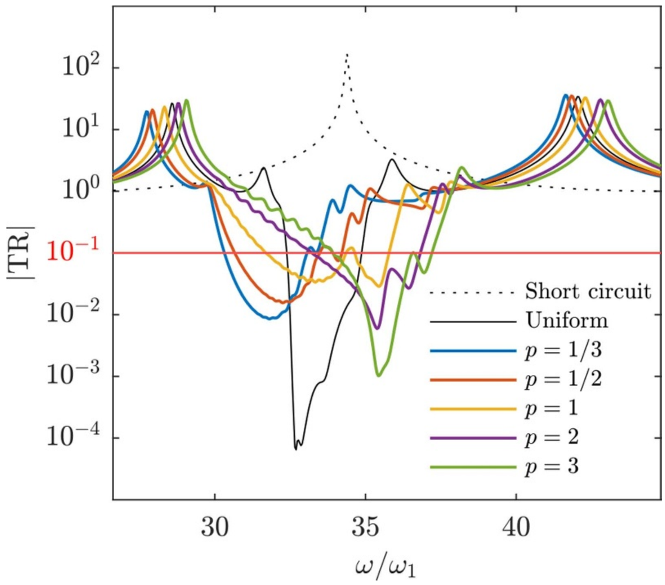

Figure 6. Tip transmissibility for different frequency grading patterns. $N = 200$, $\tau\omega_t = 100$, $\Delta\omega = 3$, $S = 25$, and $\zeta_r = 0.001$ are used.

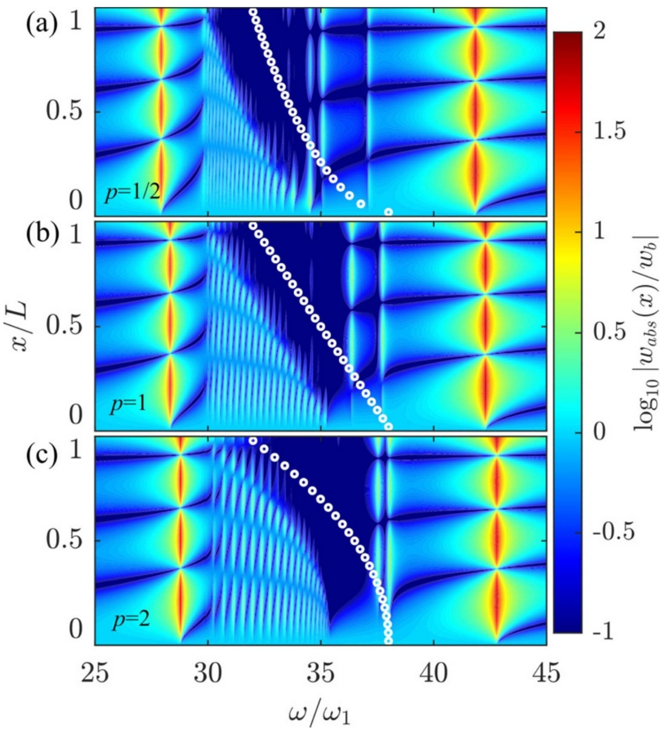

Figure 7. Displacement heatmaps versus normalized excitation frequency and dimensionless beam length for (a) fractional ($p = 1/2$), (b) first-order ($p = 1$) and (c) quadratic ($p = 2$) frequency grading patterns. (a) shows more localized vibration modes near the clamped end. $N = 200$, $\tau\omega_t = 500$, $\Delta\omega = 3$, $S = 25$, and $\zeta_r = 0.001$ are used.

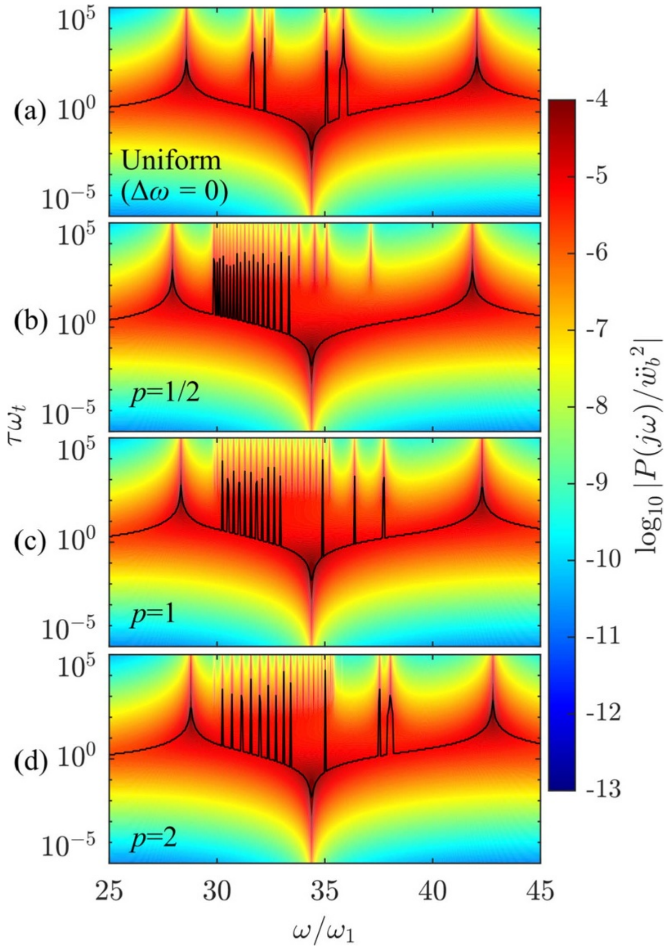

Figure 8. Real power heatmaps versus normalized excitation frequency and dimensionless load resistance for (a) uniform, (b) fractional ($p = 1/2$), (c) first-order ($p = 1$) and (d) quadratic ($p = 2$). Black line shows the optimal load resistance that maximizes the power output at each normalized excitation frequency. $\Delta\omega = 3$, $S = 25$, $N = 200$, and $\zeta_r = 0.001$ are used.

beam (near the clamped end of the beam) while the ascending one does not.

For graded locally resonant metamaterial with mechanical resonating elements, the opposite discussion is true because the bandgap is formed to the right of the target frequency [7]. Because descending graded frequency patterns display both vibration attenuation and mode localization that can be exploited to enhance the harvested energy, we therefore focus on descending graded frequency patterns for the rest of this study.

3.2. Effect of electrical load resistance

In this section, we investigate the effect of varying the electrical load resistance on the vibration attenuation of the piezoelectric metastructure with graded local resonators. Figure 5 shows the tip transmissibility versus dimensionless load resistance $\tau\omega_t$ for different frequency grading patterns. These heatmaps reveal the optimal value of the load resistance that maximizes the bandgap width (represented by the darkest blue region). One clearly observes that graded local resonators show wider bandgaps compared to the uniform resonators ($\Delta\omega = 0$). For a locally resonant metastructure with uniform resonators, it is typical to consider undamped resonators

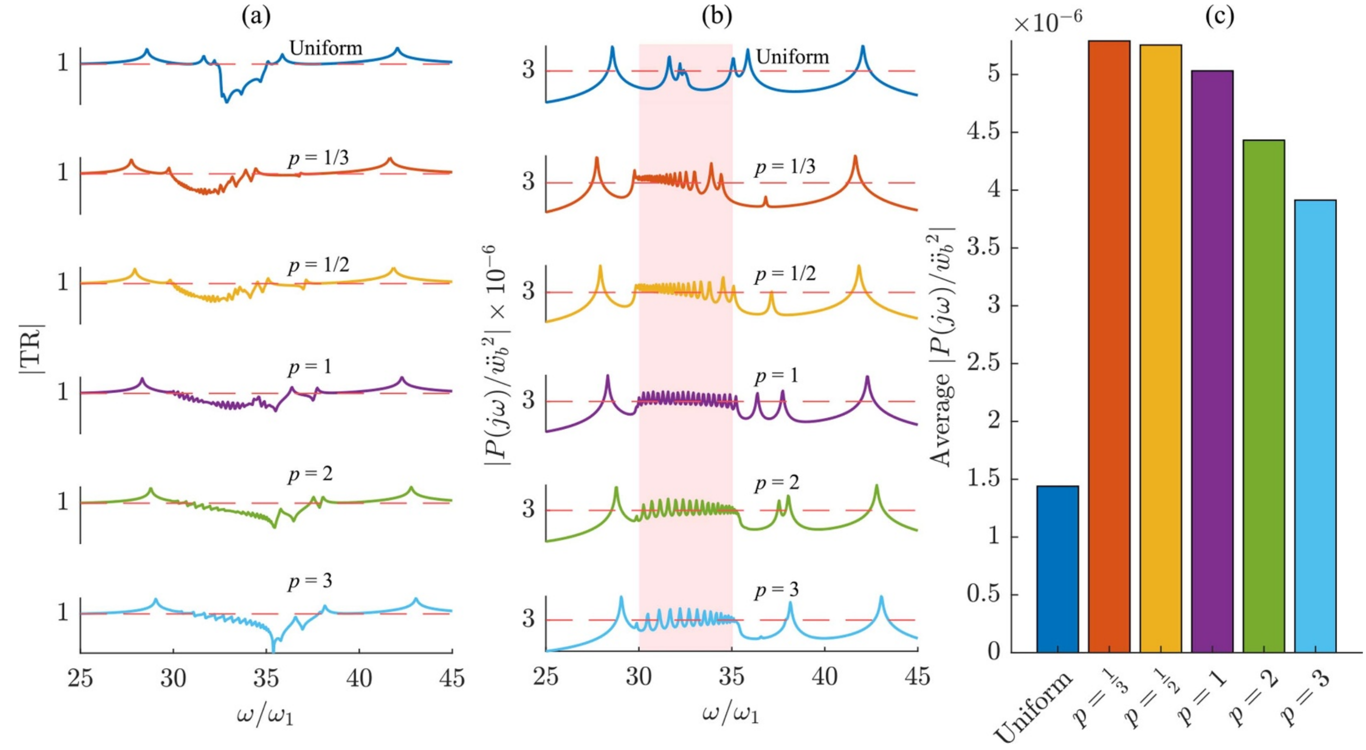

Figure 9. (a) Tip transmissibility and (b) real power output for different frequency grading patterns. (c) Average real power output computed over the normalized excitation frequency range shown as shaded region in (b). $N = 200$, $\tau\omega_t = 500$, $\Delta\omega = 3$, $S = 25$ and $\zeta_r = 0.001$.

(i.e. no load resistance in the shunts [6]), however, in the graded configuration the localized modes are very sensitive to electrical load resistance in the shunts. That is, high values of electrical load resistance (reduced damping in the resonators close to open circuit) would display more resonant peaks inside the attenuation gap for graded patterns. Therefore, some intermediate values of load resistance will be considered to have minimum resonant peaks for all graded patterns. We focus on load resistance values between $\tau\omega_t = 100$ and 500 in the following sections.

3.3. Performance comparison for vibration attenuation

In light of the previous sections, descending frequency grading patterns are superior in terms of the vibration attenuation and wave trapping capabilities in a piezoelectric metastructure. To observe the vibration attenuation enhancement, we fix the dimensionless load resistance $\tau\omega_t$ and frequency grading range $2\Delta\omega$, and compare different graded frequency patterns with the uniform case. The evaluation of vibration attenuation is based on how wide the bandgap is according to equation (24). Figure 6 shows the tip transmissibility plots for a variety of graded frequency patterns. The first-order pattern yields the widest attenuation band, but weakest vibration attenuation intensity. We observe that, as the grading order p increases, the transmissibility curve slowly dips below 0.1 (red horizontal line), and the vibration attenuation intensity increases (associated with a narrower attenuation band). The percentages of enhancement in the bandgap width for each frequency grading pattern are listed in table 3. The localized vibration modes slowly move away from the tip of the beam toward the clamped end, such that the waves are trapped over a wider spatial region (figure 7). That is, if we trace the evolution of steady wave profiles (as heatmaps versus normalized excitation frequency and dimensionless beam length) from the start to the end frequency of the bandgap, we can clearly see that the pattern of wave trapping along the beam follows the frequency grading pattern of the shunt circuits. These observations are valid for each pattern shown in figure 7. Because first-order grading pattern provides constant frequency spacing between neighboring shunt circuits, the localization of vibration modes occurs at a constant rate with respect to the excitation frequency, unlike higher-order grading patterns where the formation of localized modes occurs slowly with respect to the excitation frequency. This is interesting because when we look at the fractional grading pattern, the localization of vibration modes occurs rapidly with respect to the excitation frequency. In all cases, vibration modes appear over the entire beam length when the excitation frequency is at the start of the bandgap and gradually localized near the clamped end at the end of the bandgap. The frequency grading order (p) governs how waves localize with respect to the excitation frequency. This is particularly important when we look at the power output of shunt circuits. Having the vibration energy localized over some distance (preferably small distance) over a wide frequency excitation range enables us to extract the power more efficiently. Therefore, to localize vibration modes near the excitation point (clamped end), a fractional frequency grading pattern is the best choice as it localizes vibration modes of a wider frequency range over a short distance (near the clamped end). These remarks are

Table 3. Normalized bandgap width for different frequency grading patterns (in figure 6) and the percentage increase relative to uniform grading.

Frequency pattern	Normalized bandgap	% Increase
Uniform	2.45	0
$p = 1/3$	2.73	11.4
$p = 1/2$	3.49	42.4
$p = 1$	4.05	65.3
$p = 2$	3.53	44.1
$p = 3$	3.25	32.7

useful when it comes to energy harvesting implementation as will be shown next.

3.4. Wideband energy harvesting implications

Harvesting energy from vibrating structures is an attractive approach to power small electronic components such as sensors for structural health monitoring, among other applications [50–52]. The efficiency of the harvested energy is increased when the vibrational energy is confined at some spatial position along the structure. That is, by trapping the waves at some position and then extracting the energy using the direct piezoelectric effect is a favorable solution. For this purpose, we look at the ability to improve the real power output for different graded arrays of shunt circuits. To this end, we first show the effect of varying electrical load resistance as heatmaps of the sum of the real power output across all shunt circuits versus the normalized excitation frequency and dimensionless time constant for different frequency grading patterns as shown in figure 8. The plots show the optimal load resistance that maximizes the real power output at each excitation frequency. For all cases other than the uniform one, high power output is obtained over a wider frequency range (from 30 to 35). To evaluate the performance of the frequency grading patterns, we focus on the frequency region where localized vibration modes occur (from 30 to 35) and calculate the average power output over this region as shown in figure 9. The figure clearly shows that fractional patterns exhibit higher average power compared with the other cases. Overall, any of the graded scenarios is better than harvesting with uniform resonators when it comes to bandwidth enhancement.

4. Conclusion

In this paper, a locally resonant piezoelectric metastructure with a graded array of shunted piezoelectric patches was considered. The electromechanical equations describing the linear transverse displacement of the beam and output electric voltages were reviewed and solved using the matrix inversion method. The grading parameter was the resonance frequency of each shunt circuit; specifically, grading was performed on the inductance of shunt circuits, keeping the associated capacitance and resistance fixed. Fractional, first-order, and high-order frequency grading patterns were considered to reveal the effect of frequency grading on the vibration attenuation bandwidth, vibration localization, and harvested power. Numerical results showed that first-order frequency grading pattern resulted in the widest bandgap, yielding 65% increase in the bandwidth compared to the uniform pattern; while fractional frequency grading patterns resulted in the highest harvested power. All graded scenarios resulted in wider energy harvesting bandwidth as compared to the uniform resonators case. Also, fractional grading patterns showed wideband localization of vibration modes. The findings clearly show the significance of properly grading the resonance frequencies of the shunt circuits to achieve the desired enhancement in vibration attenuation and energy harvesting.

ORCID iDs

M Alshaqaq https://orcid.org/0000-0002-4407-8980
A Erturk https://orcid.org/0000-0003-0110-5376

References

[1] Zhengyou L, Zhang X, Mao Y, Zhu Y Y, Yang Z, Chan C T and Sheng P 2000 Locally resonant sonic materials *Science* **289** 1734–6
[2] Sheng P, Mei J, Liu Z and Wen W 2007 Dynamic mass density and acoustic metamaterials *Physica* B **394** 256–61
[3] Al Ba'ba'a H B and Mostafa N 2017 Mechanics of longitudinal and flexural locally resonant elastic metamaterials using a structural power flow approach *Int. J. Mech. Sci.* **122** 341–54
[4] Sugino C, Xia Y, Leadenham S, Ruzzene M and Erturk A 2017a A general theory for bandgap estimation in locally resonant metastructures *J. Sound Vib.* **406** 104–23
[5] Fang N, Dongjuan Xi, Jianyi X, Ambati M, Srituravanich W, Sun C and Zhang X 2006 Ultrasonic metamaterials with negative modulus *Nat. Mater.* **5** 452–6
[6] Sugino C, Leadenham S, Ruzzene M and Erturk A 2017b An investigation of electroelastic bandgap formation in locally resonant piezoelectric metastructures *Smart Mater. Struct.* **26** 055029
[7] Sugino C, Ruzzene M and Erturk A 2018 Merging mechanical and electromechanical bandgaps in locally resonant metamaterials and metastructures *J. Mech. Phys. Solids* **116** 323–33
[8] Huang G L and Sun C T 2010 Band gaps in a multiresonator acoustic metamaterial *J. Vib. Acoust.* **132** 031003
[9] De Ponti J M, Andrea C, Emanuele R, Raffaele A, Francesco B, Alberto C, and Craster R V 2020a Experimental investigation of amplification, via a mechanical delay-line, in a rainbow-based metasurface for energy harvesting arXiv:2005.04792
[10] Xiao Y, Wen J and Wen X 2012a Sound transmission loss of metamaterial-based thin plates with multiple subwavelength arrays of attached resonators *J. Sound Vib.* **331** 5408–23
[11] Kuan L, Wu J H, Jing Li, Gao N and Guan D 2017a The two-degree-of-freedom local resonance elastic metamaterial plate with broadband low-frequency bandgaps *J. Phys. D: Appl. Phys.* **50** 095104
[12] Miranda Jr E J P, Nobrega E D, Ferreira A H R and Dos Santos J M C 2019 Flexural wave band gaps in a multi-resonator elastic metamaterial plate using kirchhoff-love theory *Mech. Syst. Signal Process.* **116** 480–504

[13] Dianlong Y, Liu Y, Zhao H, Wang G and Qiu J 2006 Flexural vibration band gaps in euler-bernoulli beams with locally resonant structures with two degrees of freedom *Phys. Rev.* B **73** 064301
[14] Zhou W, You W and Zuo L 2015 Vibration and wave propagation attenuation for metamaterials by periodic piezoelectric arrays with high-order resonant circuit shunts *Smart Mater. Struct.* **24** 065021
[15] Wang G, Cheng J, Chen J and Yunze H 2017 Multi-resonant piezoelectric shunting induced by digital controllers for subwavelength elastic wave attenuation in smart metamaterial *Smart Mater. Struct.* **26** 025031
[16] Xiao Y, Wen J and Wen X 2012b Broadband locally resonant beams containing multiple periodic arrays of attached resonators *Phys. Lett.* **376** 1384–90
[17] Zhu R, Liu X N, Hu G K, Sun C T and Huang G L 2014 A chiral elastic metamaterial beam for broadband vibration suppression *J. Sound Vib.* **333** 2759–73
[18] Shuguang Z, Tianxin N, Xudong W and Jialu F 2017 Studies of band gaps in flexural vibrations of a locally resonant beam with novel multi-oscillator configuration *J. Vib. Control* **23** 1663–74
[19] Shilong Li, Jiawen X and Tang J 2017 Adaptive acoustic metamaterial with periodic piezoelectric network *Proc. SPIE Active and Passive Smart Structures and Integrated Systems 2017* (Int. Society for Optics and Photonics) 101640N
[20] Guobiao H, Tang L, Das R, Gao S and Liu H 2017 Acoustic metamaterials with coupled local resonators for broadband vibration suppression *AIP Adv.* **7** 025211
[21] Guobiao H, Tang L and Das R 2018 Internally coupled metamaterial beam for simultaneous vibration suppression and low frequency energy harvesting *J. Appl. Phys.* **123** 055107
[22] Yuan B, Humphrey V F, Wen J and Wen X 2013 On the coupling of resonance and Bragg scattering effects in three-dimensional locally resonant sonic materials *Ultrasonics* **53** 1332–43
[23] Xiao Y, Wen J, Wang G and Wen X 2013a Theoretical and experimental study of locally resonant and Bragg band gaps in flexural beams carrying periodic arrays of beam-like resonators *J. Vib. Acoust.* **135** 041006
[24] Chen Y and Wang L 2014 Periodic co-continuous acoustic metamaterials with overlapping locally resonant and Bragg band gaps *Appl. Phys. Lett.* **105** 191907
[25] Xiao Y, Wen J, Huang L and Wen X 2013b Analysis and experimental realization of locally resonant phononic plates carrying a periodic array of beam-like resonators *J. Phys. D: Appl. Phys.* **47** 045307
[26] de Sousa V C, Tan D, Marqui Jr C D and Erturk A 2018 Tunable metamaterial beam with shape memory alloy resonators: theory and experiment *Appl. Phys. Lett.* **113** 143502
[27] Chuang K-C, Xu-Feng Lv and Wang D-F 2019 A tunable elastic metamaterial beam with flat-curved shape memory alloy resonators *Appl. Phys. Lett.* **114** 051903
[28] Xiang Y, Zhenbo L, Cui F, Cheng Li and Yongdong C 2017 Tunable acoustic metamaterial with an array of resonators actuated by dielectric elastomer *Extreme Mechanics Lett.* **12** 37–40
[29] Zhenbo L, Shrestha M and Lau G-K 2017b Electrically tunable and broader-band sound absorption by using micro-perforated dielectric elastomer actuator *Appl. Phys. Lett.* **110** 182901
[30] Bortot E, Amir O and Shmuel G 2018 Topology optimization of dielectric elastomers for wide tunable band gaps *Int. J. Solids Struct.* **143** 262–73
[31] Thorp O, Ruzzene M and Baz A 2001 Attenuation and localization of wave propagation in rods with periodic shunted piezoelectric patches *Smart Mater. Struct.* **10** 979
[32] Chen S, Wang G, Wen J and Wen X 2013 Wave propagation and attenuation in plates with periodic arrays of shunted piezo-patches *J. Sound Vib.* **332** 1520–32
[33] Fang X, Wen J, Yin J and Dianlong Y 2016 Wave propagation in nonlinear metamaterial multi-atomic chains based on homotopy method *AIP Adv.* **6** 121706
[34] Fang X, Wen J, Bonello B, Yin J and Dianlong Y 2017 Ultra-low and ultra-broad-band nonlinear acoustic metamaterials *Nat. Commun.* **8** 1–11
[35] Xia Y, Ruzzene M and Erturk A 2019 Dramatic bandwidth enhancement in nonlinear metastructures via bistable attachments *Appl. Phys. Lett.* **114** 093501
[36] Xia Y, Erturk A and Ruzzene M 2020 Topological edge states in quasiperiodic locally resonant metastructures *Phys. Rev. Appl.* **13** 014023
[37] Tsakmakidis K L, Boardman A D and Hess O 2007 trapped rainbow' storage of light in metamaterials *Nature* **450** 397–401
[38] Gan Q, Gao Y, Wagner K, Vezenov D, Ding Y J and Bartoli F J 2011 Experimental verification of the rainbow trapping effect in adiabatic plasmonic gratings *Proc. Natl Acad. Sci.* **108** 5169–73
[39] Zhu J, Chen Y, Zhu X, Garcia-Vidal F J, Yin X, Zhang W and Zhang X 2013 Acoustic rainbow trapping *Sci. Rep.* **3** 1728
[40] Cardella D, Celli P and Gonella S 2016 Manipulating waves by distilling frequencies: a tunable shunt-enabled rainbow trap *Smart Mater. Struct.* **25** 085017
[41] Airoldi L and Ruzzene M 2011 Design of tunable acoustic metamaterials through periodic arrays of resonant shunted piezos *New J. Phys.* **13** 113010
[42] Bergamini A E, Zündel M, Flores Parra E A, Delpero T, Ruzzene M and Ermanni P 2015 Hybrid dispersive media with controllable wave propagation: a new take on smart materials *J. Appl. Phys.* **118** 154310
[43] Wang G and Chen S 2015 Large low-frequency vibration attenuation induced by arrays of piezoelectric patches shunted with amplifier–resonator feedback circuits *Smart Mater. Struct.* **25** 015004
[44] Sugino C, Ruzzene M and Erturk A 2020 Digitally programmable resonant elastic metamaterials *Phys. Rev. Appl.* **13** 061001
[45] Thomas O, Ducarne J and Deü J-Fçois 2011 Performance of piezoelectric shunts for vibration reduction *Smart Mater. Struct.* **21** 015008
[46] Guobiao H, Austin A C M, Sorokin V and Tang L 2021 Metamaterial beam with graded local resonators for broadband vibration suppression *Mech. Syst. Signal Process.* **146** 106982
[47] De Ponti J M, Colombi A, Ardito R, Braghin F, Corigliano A and Craster R V 2020b Graded elastic metasurface for enhanced energy harvesting *New J. Phys.* **22** 013013
[48] Chaplain G J, Pajer D, De Ponti J M and Craster R V 2020 Rainbow reflection and trapping for energy harvesting arXiv:2002.05260
[49] Celli P, Yousefzadeh B, Daraio C and Gonella S 2019 Bandgap widening by disorder in rainbow metamaterials *Appl. Phys. Lett.* **114** 091903
[50] Anton S R and Sodano H A 2007 A review of power harvesting using piezoelectric materials (2003–2006) *Smart Mater. Struct.* **16** R1
[51] Safaei M, Sodano H A and Anton S R 2019 A review of energy harvesting using piezoelectric materials: state-of-the-art a decade later (2008–2018) *Smart Mater. Struct.* **28** 113001
[52] Erturk A and Inman D J 2011 *Piezoelectric Energy Harvesting* (New York : Wiley)